

# Synergistic Interlayer and Defect Engineering in VS<sub>2</sub> Nanosheets toward Efficient Electrocatalytic Hydrogen Evolution Reaction

Junjun Zhang, Chenhui Zhang, Zhenyu Wang, Jian Zhu, Zhiwei Wen, Xingzhong Zhao, Xixiang Zhang,\* Jun Xu,\* and Zhouguang Lu\*

A simple one-pot solvothermal method is reported to synthesize VS<sub>2</sub> nanosheets featuring rich defects and an expanded (001) interlayer spacing as large as 1.00 nm, which is a ≈74% expansion as relative to that (0.575 nm) of the pristine counterpart. The interlayer-expanded VS<sub>2</sub> nanosheets show extraordinary kinetic metrics for electrocatalytic hydrogen evolution reaction (HER), exhibiting a low overpotential of 43 mV at a geometric current density of 10 mA cm<sup>-2</sup>, a small Tafel slope of 36 mV dec<sup>-1</sup>, and long-term stability of 60 h without any current fading. The performance is much better than that of the pristine VS<sub>2</sub> with a normal interlayer spacing, and even comparable to that of the commercial Pt/C electrocatalyst. The outstanding electrocatalytic activity is attributed to the expanded interlayer distance and the generated rich defects. Increased numbers of exposed active sites and modified electronic structures are achieved, resulting in an optimal free energy of hydrogen adsorption ( $\Delta G_{\text{H}}$ ) from density functional theory calculations. This work opens up a new door for developing transition-metal dichalcogenide nanosheets as high active HER electrocatalysts by interlayer and defect engineering.

## 1. Introduction

Electrochemical water splitting is an approach to produce H<sub>2</sub> from water with electricity power. Hydrogen evolution reaction (HER) plays a pivotal role in the electrochemical water splitting. Active electrocatalysts, such as platinum (Pt) and its alloys, have been known as the state-of-the-art HER catalysts, however, their practical applications are severely hindered by their high cost and scarce natural reserves. Therefore, searching for earth-abundant and non-noble catalysts is of great significance. Efficient and robust electrocatalysts are required to lower reaction overpotential and minimize energy consumption. Recently, extensive research efforts have been devoted to exploring high-performance and non-noble metal HER electrocatalysts.<sup>[1–3]</sup>


Numerous 2D layered transition-metal dichalcogenide (MX<sub>2</sub>) nanosheets, such as MoS<sub>2</sub>, WS<sub>2</sub>, MoSe<sub>2</sub>, WSe<sub>2</sub>, have received considerable attention owing to their high catalytic activity and low cost.<sup>[4–6]</sup> Considerable efforts have been devoted to MX<sub>2</sub> nanosheets as advanced HER electrocatalysts. Both theoretical and experimental studies have pointed out that the edges of the MX<sub>2</sub> nanosheets are active but the basal planes are inert. Several merits such as high conductivity, high activity, and durable stability are required for the active electrocatalysts. Three strategies have been developed to improve the HER performance: (i) To improve the conductivity (by means of conductive carbon modification, doping, or phase engineering). For example, the phase transition of MX<sub>2</sub> nanosheets from semiconducting 2H phase to metallic 1T phase could lead to significant improvement of HER activity.<sup>[7–10]</sup> However, the metallic 1T phase is metastable, thus it may be hard to achieve outstanding long-term stability. (ii) To increase the exposed edge density (by generating more defects, disorders, or making vertical aligned MX<sub>2</sub> nanosheets).<sup>[11–15]</sup> (iii) Interlayer expansion is recently expected as a new approach to increase HER activity, as it can offer varied electronic structure and optimized free energy of hydrogen adsorption ( $\Delta G_{\text{H}}$ ).<sup>[16–19]</sup> Interlayer-expanded MoS<sub>2</sub> and MoSe<sub>2</sub> nanosheets have been recently demonstrated to show significantly enhanced HER performance.<sup>[20,21]</sup> Therefore, integrating these advantages to develop robust electrocatalysts is of great significance, but full of challenges.

Dr. J. Zhang, Z. Wang, J. Zhu, Z. Wen, Prof. Z. Lu  
Shenzhen Key Laboratory of Hydrogen Energy  
and Department of Materials Science and Engineering  
Southern University of Science and Technology  
Shenzhen 518055, P. R. China  
E-mail: luzg@sustc.edu.cn

Dr. J. Zhang, Prof. X. Zhao  
School of Physics and Technology  
Wuhan University  
Wuhan 430072, P. R. China

Prof. J. Xu  
School of Electronic Science and Applied Physics  
Hefei University of Technology  
Hefei 230009, P. R. China  
E-mail: apjunxu@hfut.edu.cn

C. Zhang, Prof. X. Zhang  
Physical Sciences and Engineering Division  
King Abdullah University of Science and Technology  
Thuwal 23955-6900, Saudi Arabia  
E-mail: xixiang.zhang@kaust.edu.sa

 The ORCID identification number(s) for the author(s) of this article can be found under <https://doi.org/10.1002/sml.201703098>.

DOI: 10.1002/sml.201703098

VS<sub>2</sub> is considered as a promising candidate for HER as it is an intrinsic metallic transition-metal dichalcogenide (TMD) and has a similar layered structure to MoS<sub>2</sub>.<sup>[22,23]</sup> Given that the stable structure and the high conductivity favoring fast electron transport, metallic VS<sub>2</sub> with delicate nanostructures would be a potentially superior HER electrocatalyst. Theoretical studies have revealed that metallic VS<sub>2</sub> monolayers exhibit superior HER activity among other TMDs, and catalytic activity of VS<sub>2</sub> nanostructures strongly depends on edge structure and configuration.<sup>[24–26]</sup> Recently, morphology tuning of VS<sub>2</sub> nanostructures and their composites have been experimentally conducted to improve their HER performance.<sup>[27–29]</sup> To the best of our knowledge, interlayer expansion and defect engineering of VS<sub>2</sub> nanostructures for improving their HER activity have never been investigated. In this work, we report a facile one-pot solvothermal route to synthesize microflowers consisting of tiny VS<sub>2</sub> nanosheets. The metallic VS<sub>2</sub> nanosheets possess rich defects, and exhibit a considerably expanded (001) interlayer spacing as large as 1.00 nm with a 74% expansion as compared to that (0.575 nm) of the bulk counterpart. The defect-rich and interlayer-expanded VS<sub>2</sub> nanosheets show significantly improved HER performance, even comparable to that of the commercial Pt/C catalyst. Our work provides a promising way to develop robust and advanced HER catalysts through interlayer expansion and defect modulation.

## 2. Results and Discussion

Interlayer-expanded VS<sub>2</sub> nanosheets were prepared by reacting ammonium vanadate with thioacetamide in an *n*-octylamine solvent through a one-pot solvothermal route. From the low-magnification scanning electron microscopy (SEM) image in Figure 1a, it is found that the freshly prepared VS<sub>2</sub> is composed of uniform microflower-like structures with diameters of ≈2 μm. Figure 1b shows a magnified SEM image, which reveals that the microflowers are actually assembled from numerous thin nanosheets. Transmission electron microscopy (TEM) observation in Figure 1c further confirms that the hierarchical structures are constructed from numerous VS<sub>2</sub> nanosheets. Figure 1d presents a TEM image of a flat-lying VS<sub>2</sub> nanosheet and a corresponding selected-area electron diffraction (SAED) pattern inset revealing its polycrystalline nature with concentric rings. An energy dispersive X-ray (EDX) spectrum is displayed in Figure S1a (Supporting Information), which reveals the existence of V and S elements in the nanosheets. EDX elemental mappings in Figure S1b (Supporting Information) further indicate homogeneous distribution of the two elements throughout the microflowers. Figure 1e shows a high-resolution TEM (HRTEM) image of the freshly prepared VS<sub>2</sub> nanosheets. The thickness of the layered nanosheets is estimated to be about 10–15 nm. The interlayer spacing between two adjacent monolayers is as large as 1.00 nm, corresponding to expanded (001) interplanar spacing along *c*-axis direction. It exhibits a ≈74% expansion as compared to that (0.575 nm) of the pristine bulk VS<sub>2</sub>. The phenomenon of interlayer expansion has often been observed in layered MoS<sub>2</sub> and MoSe<sub>2</sub> nanosheets.<sup>[19–22,30]</sup> Along with the expanded interlayer spacing, a lot of intrinsic defects marked with yellow arrows could also be observed, which may

have resulted from the disordered structure of lattice expansion. The atomic arranging manners on the basal surface are strongly disordered (Figure 1e), in which even short-range ordering of nanodomains could not be clearly observed. A fast Fourier transform (FFT) pattern of the basal surface is shown in the inset of Figure 1e. The closed diffraction rings further support the disordered arrangement of nanodomains. These results demonstrate the formation of several layered VS<sub>2</sub> nanosheets with enlarged interlayer spacings and rich defects.

Figure 2a shows X-ray diffraction (XRD) patterns of the solvothermal VS<sub>2</sub> nanosheets before and after annealing. For the freshly prepared solvothermal sample, the diffraction peaks are significantly different from those of pristine VS<sub>2</sub> (JCPDF 89-1640). Two new sharp diffraction peaks at  $2\theta = 8.7^\circ$  and  $17.6^\circ$  corresponding to the *d*-spacing of 1.00 and 0.50 nm are observed, and can be indexed into expanded (001) and (002) planes of VS<sub>2</sub>, respectively. These two peaks with a diploid relationship are diffractions from a series of (00*l*) Bragg peaks from a layered structure.<sup>[21]</sup> The relationship of doubling interplanar distance (1.00 nm = 0.50 nm × 2) reveals the formation of lamellar stacking along *c*-axis of the S–V–S sandwiched monolayer with an expanded interlayer spacing of 1.00 nm.<sup>[30]</sup> Compared with bulk VS<sub>2</sub>, the distinct shift of (001) peak to lower  $2\theta$  degree suggests a substantially expanded interlayer spacing from 0.575 to 1.00 nm. Origins of new (001) and (002) sharp peaks of the freshly prepared VS<sub>2</sub> sample could be attributed to lattice expansion along *c*-axis induced by octylamine intercalation. After thermal treatment at 400 °C, the intercalated-octylamine species can be effectively evaporated from the VS<sub>2</sub> nanosheets. It is observed that all the diffraction peaks of the annealed solvothermal VS<sub>2</sub> sample match well with those of the pristine VS<sub>2</sub> (JCPDF 89-1640). The (001) and (002) diffraction peaks of the annealed VS<sub>2</sub> sample moved into normal position, thus indicating its restored interlayer spacing. The interlayer spacing of the annealed VS<sub>2</sub> nanosheets is confirmed by HRTEM analysis to be 0.57 nm (Figure S2, Supporting Information), which is very close to the value of pristine bulk VS<sub>2</sub>. The annealed VS<sub>2</sub> still maintains the nanosheet morphology. A more regular atomic arrangement on the basal surface is observed. The lattice spacing of 0.278 nm matches well with the (100) interplanar spacing of hexagonal VS<sub>2</sub>, indicating the significantly decreased defects in these annealed VS<sub>2</sub> nanosheets.

Figure 2b shows the Raman spectra of the freshly prepared and the annealed solvothermal VS<sub>2</sub> samples. Both of them show two characteristic peaks located, respectively, at 280 cm<sup>-1</sup> due to the E<sub>g</sub> mode resulted from the V–S in-plane vibration and at 403 cm<sup>-1</sup> due to the out-of-plane A<sub>g</sub> vibration.<sup>[27,31]</sup> Two additional broad overlapping bands at ≈1365 cm<sup>-1</sup> (disorder-induced D-band) and 1580 cm<sup>-1</sup> (graphitic G-band) are also observed for both the freshly prepared and the annealed VS<sub>2</sub>. It reveals the presence of disordered and amorphous carbon, which resulted from carbonization of octylamine under the solvothermal condition.<sup>[32]</sup>

X-ray photoelectron spectroscopy (XPS) was further performed to probe the elemental composition and chemical state of the freshly prepared and the annealed solvothermal VS<sub>2</sub> samples. Figure 3a shows V 2p core level spectra. Both spectra can be fitted with two sets of doublet peaks. The doublet peaks at the higher binding energy of 523.9 and 516.6 eV are

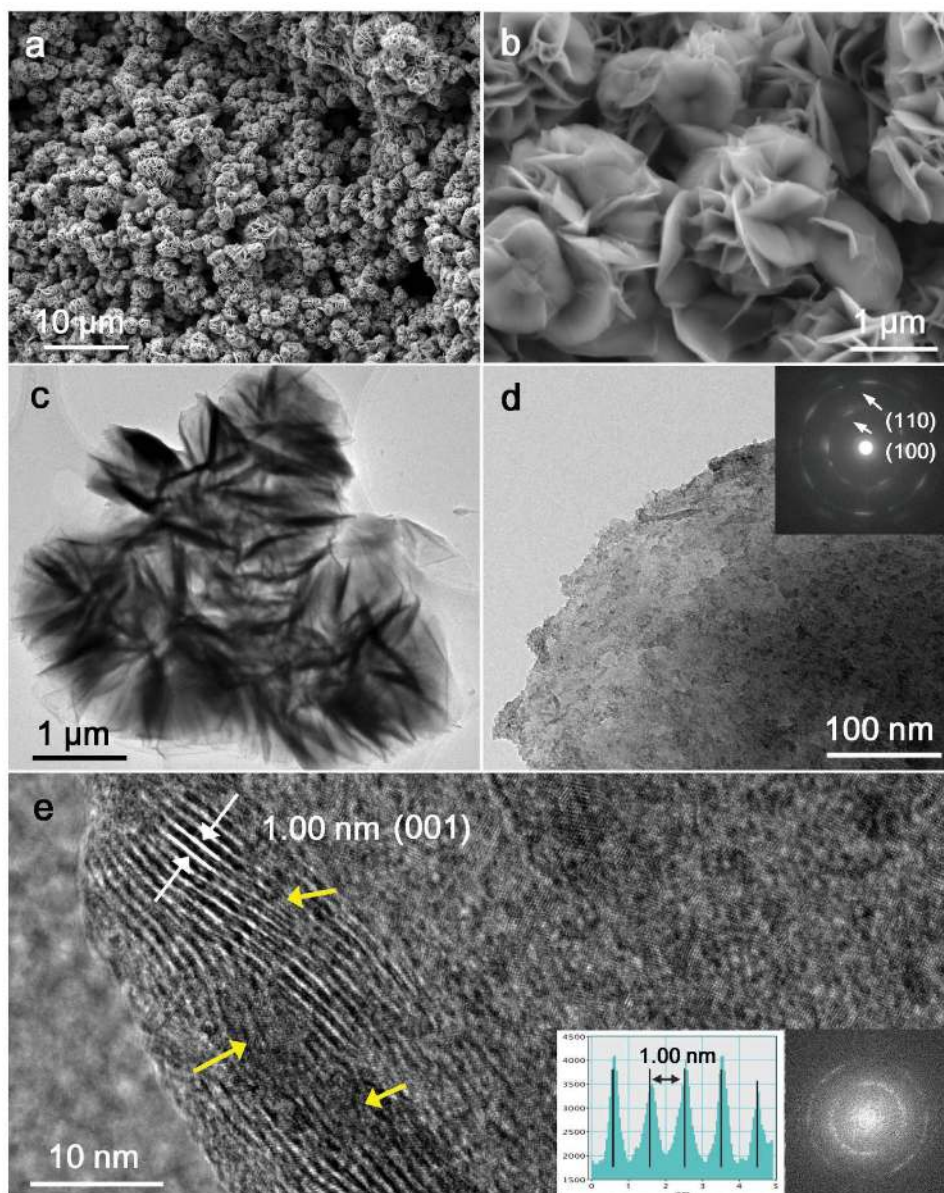


**Figure 1.** a,b) SEM images of the freshly prepared  $\text{VS}_2$  nanosheets via solvothermal synthesis. c,d) TEM images of the freshly prepared solvothermal  $\text{VS}_2$  nanosheets, inset in (d) is the corresponding SAED pattern. e) High-resolution TEM image of the freshly prepared  $\text{VS}_2$  nanosheets, showing expanded (001) interlayer spacings. Insets are the profile plot of the calibration for measuring the spacings and the corresponding FFT pattern.

attributed to V  $2p_{1/2}$  and V  $2p_{3/2}$ , indicating the  $\text{V}^{4+}$  chemical state. They are in good agreement with the reported values of  $\text{VS}_2$ .<sup>[33]</sup> The doublet peaks at the lower binding energy of 521.4 and 513.8 eV correspond to  $\text{V}^{2+}$  state.<sup>[34,35]</sup> Figure 3b shows S 2p core level spectra of the two samples. Two prominent peaks located at 162.3 and 161.1 eV can be assigned to S  $2p_{1/2}$  and S  $2p_{3/2}$  of  $\text{S}^{2-}$ .<sup>[17]</sup> Two weak peaks at higher binding energy 163.8 and 162.4 eV are attributed to the presence of metal–sulfur and sulfur ion in a low coordination state, respectively.<sup>[36]</sup> The peak at around 168.4 eV that can be assigned to sulfate is also observed for two samples, which indicates slight oxidation of the  $\text{VS}_2$  nanosheets owing to exposure to air. Figure 3c depicts the C 1s spectra of the two samples. They show similar profiles

with an asymmetric peak, which can be divided into four peaks as C–C ( $\text{sp}^2$ ), C–N, C–O, and C=O bond.<sup>[30]</sup> The observation confirms that amorphous carbon is formed in the  $\text{VS}_2$  samples as a result of carbonization of octylamine molecules during the solvothermal process. N 1s spectra are displayed in Figure 3d. The N 1s spectra can be fitted into two peaks centered at 401.9 and 399.7 eV, suggesting the presence of N–H bond from octylamine molecules (and/or  $\text{NH}_4^+$  ions) and N–C bond from N-doped amorphous carbon.<sup>[37]</sup> N signal intensity at 401.9 eV of the annealed solvothermal  $\text{VS}_2$  sample is significantly decreased, which indicates that the intercalated octylamine molecules and/or amino species were mostly removed by post-thermal treatment. In order to further confirm the intercalated

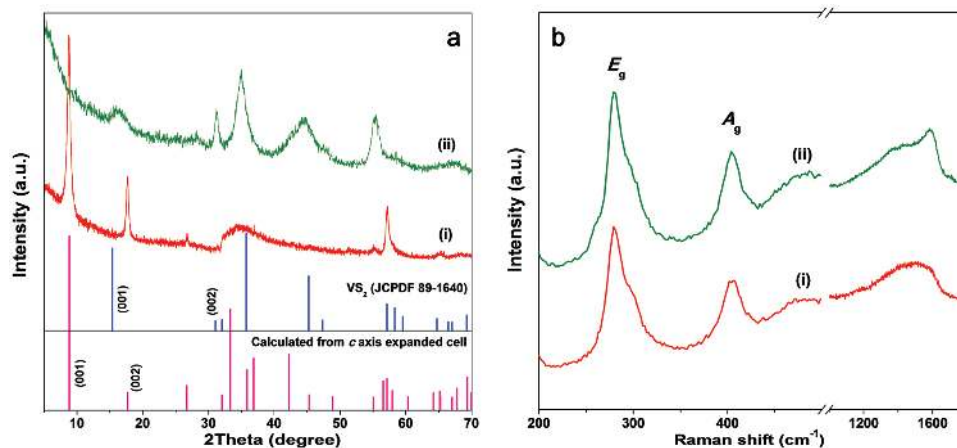


**Figure 2.** a) XRD patterns and b) Raman spectra of (i) the freshly prepared solvothermal VS<sub>2</sub> nanosheets and (ii) the annealed solvothermal VS<sub>2</sub> sample obtained by post-thermal treatment at 400 °C. The calculated pattern from *c*-axis expanded VS<sub>2</sub> cell and the standard pattern of the pristine VS<sub>2</sub> (JCPDF 89-1640) are shown as references.

species, thermogravimetric analysis (TGA) and differential scanning calorimetry (DSC) measurements of the two samples were carried out. As shown in Figure S3a (Supporting Information), the freshly prepared sample presents a much larger weight loss compared with the annealed one. The DSC curve of the freshly prepared VS<sub>2</sub> in Figure S3b (Supporting Information) shows several obvious endothermic peaks at 70, 94, 203, and 266 °C, respectively, corresponding to the mass losses. The low-temperature peaks are ascribed to the adsorbed water and

inserted NH<sub>3</sub> molecules, and the other two high-temperature peaks can be attributed to the inserted NH<sub>4</sub><sup>+</sup> ions and octylamine molecules, respectively.<sup>[38–40]</sup> In addition, the elemental analysis from EDX and XPS results for the freshly prepared solvothermal VS<sub>2</sub> nanosheets shows that the molar ratio of V:S is 1:1.9, which is close to 1:2. The slight S deficiency may be responsible for the rich defects in the sample.

To better understand the formation mechanism of inter-layer-expanded VS<sub>2</sub> nanosheets by solvothermal synthesis,

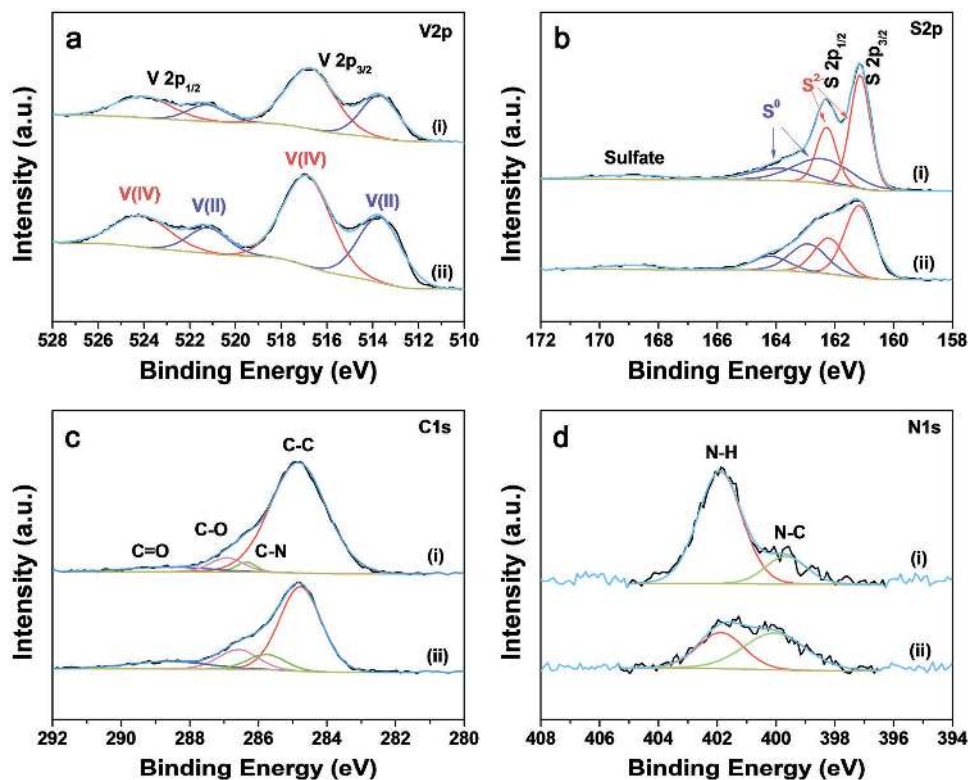


**Figure 3.** High-resolution core-level XPS spectra for a) V 2p, b) S 2p, c) C 1s, and d) N 1s core levels and corresponding peaking fitting analysis of (i) the freshly prepared solvothermal VS<sub>2</sub> nanosheets and (ii) the annealed solvothermal VS<sub>2</sub> nanosheets.

VS<sub>2</sub> nanosheets are synthesized by a hydrothermal method at the same conditions (160 °C and 24 h) as a comparison. **Figure 4a** shows a SEM image of the hydrothermal product, revealing a general morphology of nanosheets. **Figure 4b** presents an HRTEM image of the nanosheets. They have an interlayer spacing of 0.59 nm, close to the normal (001) interplanar of pristine VS<sub>2</sub> (0.575 nm). Disordered atomic arrangement in the basal surface is observed, which indicates rich defects of the hydrothermal VS<sub>2</sub> nanosheets. XRD pattern of the hydrothermal product is shown in **Figure 4c**. All the diffraction peaks in the pattern can be indexed to the hexagonal VS<sub>2</sub> (JCPDF 89-1640) with lattice constants of  $a = b = 0.322 \text{ \AA}$  and  $c = 0.575 \text{ \AA}$ , further confirming the formation of VS<sub>2</sub> nanosheets with

normal interlayer spacing. A Raman spectrum of the hydrothermal VS<sub>2</sub> nanosheets exhibits two response peaks at 280 and 403 cm<sup>-1</sup> corresponding to the E<sub>g</sub> and A<sub>g</sub> modes, respectively (**Figure 4d**). No peaks from amorphous carbon are detected. Moreover, the V 2p XPS spectrum in **Figure 4e** reveals that V exists mainly in V<sup>4+</sup> coupled with a small amount of V<sup>2+</sup>; the S 2p core levels XPS spectrum in **Figure 4f** indicates that S has a chemical valance of -2, contaminated with a small amount of elemental S and sulfate owing to slight oxidation on exposure to air. These XPS observations of the hydrothermal VS<sub>2</sub> are consistent with those of the solvothermal VS<sub>2</sub> nanosheets. All these results demonstrate the formation of rich-defect VS<sub>2</sub> nanosheets with normal interlayer spacing under hydrothermal

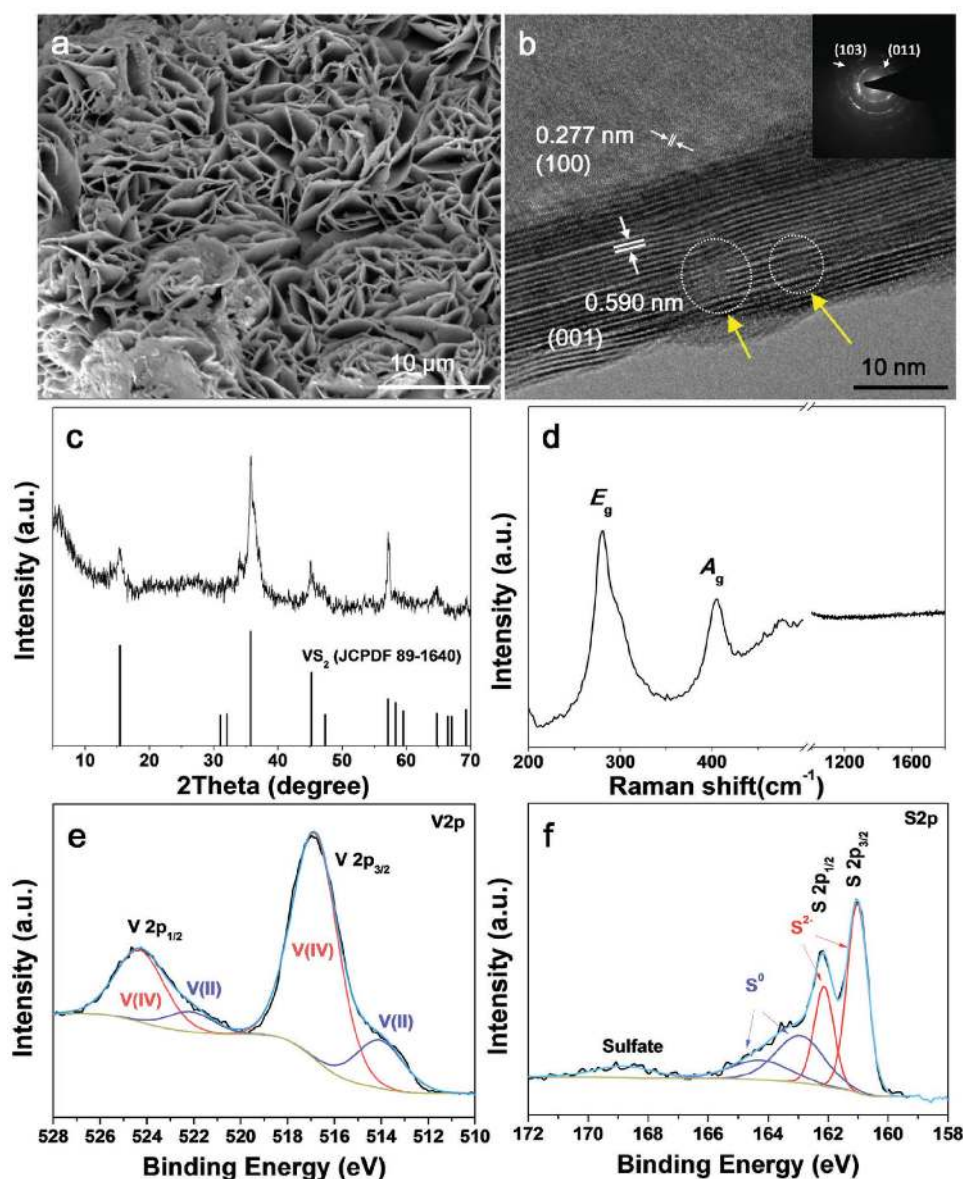


**Figure 4.** a) SEM, b) TEM images, c) XRD pattern, d) Raman spectrum, and high-resolution XPS spectra for e) V 2p and f) S 2p core levels and corresponding peaking fitting analysis of the freshly prepared VS<sub>2</sub> nanosheets via a hydrothermal method.

conditions. It may support our deduction that the octylamine intercalation is responsible for the interlayer-expanded VS<sub>2</sub> nanosheets by solvothermal synthesis.

Influences of interlayer expansion and intrinsic defect engineering on the electrocatalytic HER activities of the various

VS<sub>2</sub> nanosheets (freshly prepared solvothermal VS<sub>2</sub>, annealed solvothermal VS<sub>2</sub>, and hydrothermal VS<sub>2</sub>) are carefully investigated. Electrochemical performance of the samples coated on glassy carbon electrodes was evaluated in H<sub>2</sub>SO<sub>4</sub> solutions (0.5 M) using a typical three-electrode configuration. **Figure 5** a

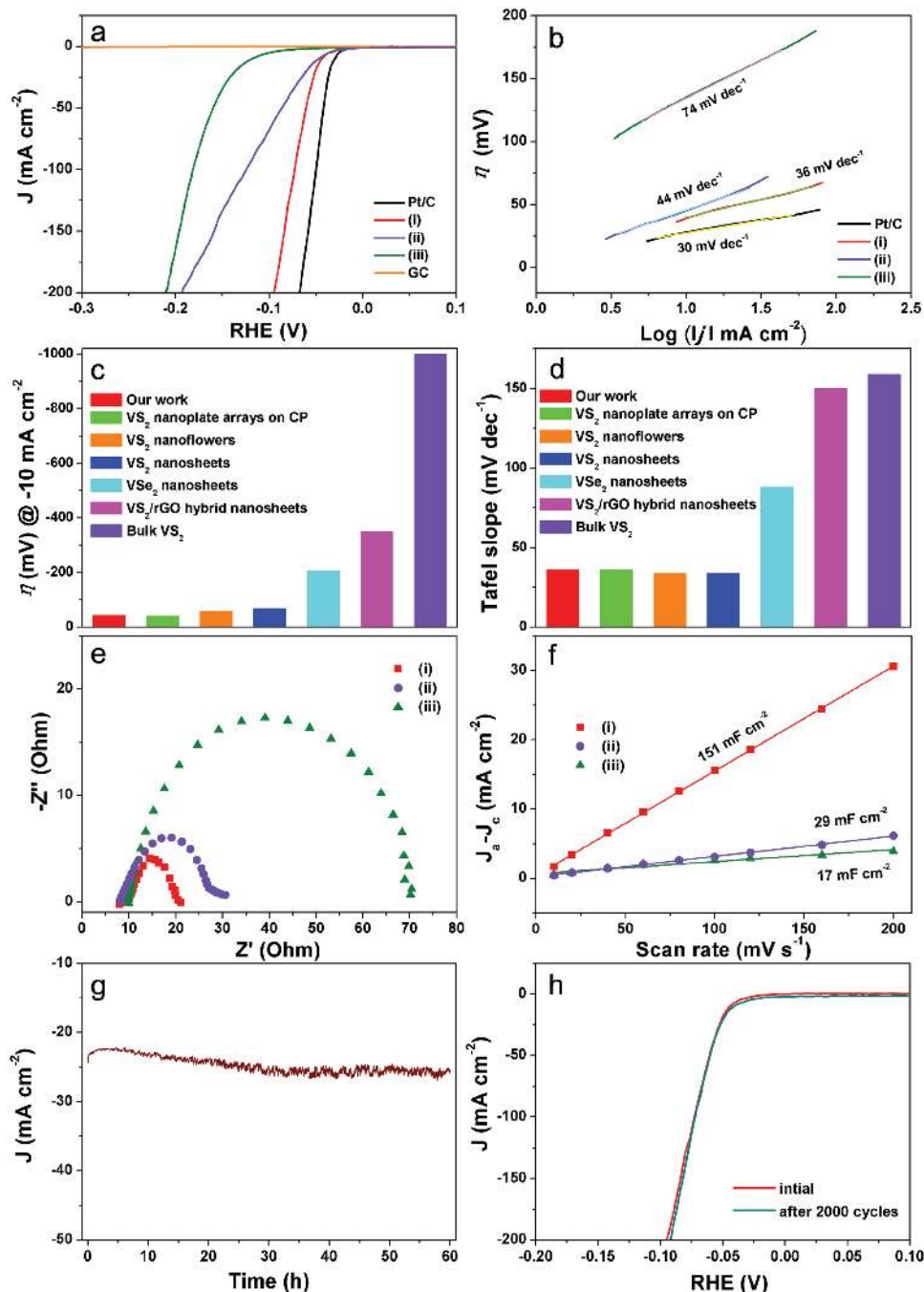


**Figure 5.** Electrochemical property of (i) the freshly prepared solvothermal VS<sub>2</sub> nanosheets, (ii) the hydrothermal VS<sub>2</sub> nanosheets, (iii) the annealed solvothermal VS<sub>2</sub> nanosheets samples for HER in 0.5 M H<sub>2</sub>SO<sub>4</sub>. a) Polarization curves at a scan rate of 5 mV s<sup>-1</sup>. b) Corresponding Tafel plots of the samples. c) Comparison of η required to generate a current density of 10 mA cm<sup>-2</sup> on various V-based catalysts. d) Comparison of Tafel slope on various V-based catalysts. e) EIS Nyquist plots of different VS<sub>2</sub> samples. f) The differences in current density variation (J<sub>a</sub> - J<sub>c</sub>) at 0.22 V versus RHE plotted against scan rate fitted to a linear regression for estimation of C<sub>dl</sub>. g) Chronoamperometric responses (J-t) recorded from the freshly prepared solvothermal VS<sub>2</sub> at a constant overpotential of -55 mV. h) Polarization curves recorded from the freshly prepared solvothermal VS<sub>2</sub> nanosheets at a scan rate of 10 mV s<sup>-1</sup> before and after 2000 cycles.

shows polarization curves of the various VS<sub>2</sub> catalysts as well as the Pt/C commercial catalyst measured with a scan rate of 5 mV s<sup>-1</sup>. All the potentials were calibrated to a reversible hydrogen electrode (RHE). The featureless polarization curve for bare glassy carbon guarantees a minimal background. Significantly, the freshly prepared solvothermal VS<sub>2</sub> catalyst shows a high HER activity as indicated by the near zero onset overpotential ( $\eta$ ) and the fast rising cathodic current at more negative potentials, which is close to that of the commercial Pt/C catalyst. The overpotentials required to drive geometric current densities of -10 mA cm<sup>-2</sup> on the freshly prepared solvothermal VS<sub>2</sub> catalysts is only 43 mV, which is much smaller than those of the hydrothermal VS<sub>2</sub> (47 mV) and the annealed solvothermal VS<sub>2</sub> catalyst (118 mV). The dependence of the logarithmic current density on  $\eta$  ( $\log J - \eta$ ) was plotted to elucidate the HER kinetics, where  $\eta$  and  $J$  are the overpotential and the generated current density, respectively. The linear relationship of  $\log J$  and  $\eta$  represents useful kinetic metrics of above catalysts, namely the Tafel slope. The Tafel slope of 36 mV dec<sup>-1</sup> was measured for the freshly prepared solvothermal VS<sub>2</sub> nanosheets. This value is much smaller than those of the hydrothermal and the annealed solvothermal catalysts, and is comparable to that of the state-of-the-art Pt/C catalyst (Figure 5b). The  $\eta$  needed to drive geometric current density of -10 mA cm<sup>-2</sup> and Tafel slopes of the reported various V-based catalysts are summarized in Figure 5c,d and Table S1 (Supporting Information). In our work, the freshly prepared solvothermal VS<sub>2</sub> catalyst exhibits a low  $\eta$  of 43 mV and a small Tafel slope of 36 mV dec<sup>-1</sup>, which performs among the best of the documented V-based catalysts. Electrochemical impedance spectroscopy (EIS) technique was carried out to provide further insight into the electrode kinetics under HER process. The Nyquist plots of the various VS<sub>2</sub> catalysts are shown in Figure 5e. The charge transfer resistance ( $R_{ct}$ ) is estimated to be 13  $\Omega$  for the freshly prepared solvothermal VS<sub>2</sub> catalyst, 20  $\Omega$  for the hydrothermal VS<sub>2</sub> catalyst, and 60  $\Omega$  for the annealed solvothermal VS<sub>2</sub> catalyst. The smallest value of the freshly prepared solvothermal VS<sub>2</sub> catalyst indicates its fast electrocatalytic Faradaic process and thus a superior HER kinetics.

N<sub>2</sub> adsorption-desorption isotherm curves and Brunauer-Emmett-Teller (BET) surface areas of the three samples are measured and presented in Figure S4 (Supporting Information). The BET surface area is 29.011 m<sup>2</sup> g<sup>-1</sup> for the freshly prepared solvothermal VS<sub>2</sub> nanosheets and 27.337 m<sup>2</sup> g<sup>-1</sup> for the annealed solvothermal VS<sub>2</sub> nanosheets. Postannealing treatment has little influence on the BET surfaces of the VS<sub>2</sub> samples. However, the hydrothermal VS<sub>2</sub> nanosheets have a much smaller BET surface area of 8.449 m<sup>2</sup> g<sup>-1</sup>, which is attributed to the large size of VS<sub>2</sub> nanosheets obtained by the hydrothermal method. Nevertheless, the HER performance of the electrocatalysts is affected not only by the surface area, but also by the active sites. Therefore, the electrochemically active surface area (ECSA) is considered as an indicator to catalytic activity of the electrocatalysts. ECSA was conducted by using a simple cyclic voltammetry method under non-Faradaic potential, as shown in Figure S5 (Supporting Information). The electrochemical double-layer capacitance ( $C_{dl}$ ), which is proportional to ECSA, was further measured as shown in Figure 5f. The  $C_{dl}$  values are 151 mF cm<sup>-2</sup> for the freshly prepared solvothermal

VS<sub>2</sub>, 17 mF cm<sup>-2</sup> for the annealed solvothermal VS<sub>2</sub>, and 29 mF cm<sup>-2</sup> for the hydrothermal VS<sub>2</sub>. As compared to the annealed solvothermal VS<sub>2</sub> nanosheets, the freshly prepared solvothermal VS<sub>2</sub> sample shows a similar BET surface area but a much larger  $C_{dl}$  value. This observation indicates that the freshly prepared solvothermal VS<sub>2</sub> sample contains high defect-induced exposed active edge sites and consequently results in the significantly enhanced HER performance. On the other hand, the hydrothermal VS<sub>2</sub> sample has a smaller BET surface area but a larger  $C_{dl}$  value than the annealed solvothermal VS<sub>2</sub> sample. As a result, the hydrothermal VS<sub>2</sub> sample exhibits obviously increased HER activity.

Long-term HER stability is another key parameter of high-performance electrocatalysts. We further evaluated the stability of the freshly prepared solvothermal VS<sub>2</sub> catalyst by a constant overpotential measurement. This quasiaelectrolysis process was conducted at a constant  $\eta$  of -55 mV in 0.5 M H<sub>2</sub>SO<sub>4</sub> (Figure 5g). Remarkably, the H<sub>2</sub> evolution can proceed at a sustained current density of -25 mA cm<sup>-2</sup> even over 60 h of continuous operation, suggesting its excellent stability. The stable stability was further proved by a long-term cycling test of polarization curves operating in the same electrolyte (Figure 5h). Negligible current losses can be observed after 2000 cycles relative to the initial one. The VS<sub>2</sub> catalyst before and after HER test is further characterized by SEM and Raman analyses as shown in Figure S6 (Supporting Information). It is revealed that the catalyst after HER test can well reserve its original morphology and composition, indicating its good structural stability.

The superior catalytic activity and kinetics of the freshly prepared solvothermal VS<sub>2</sub> nanosheets are believed to originate from synergetic advantages of expanded interlayer spacing and defect-rich structure, as illustrated in Figure 6a. On the one hand, the generated defects on the basal planes can be expected to increase the exposure of active edge sites, which dramatically improve the electrocatalytic performance.<sup>[11,42,43]</sup> On the other hand, the expanded interlayer distance can bring beneficial structural and electronic modulations, enabling each VS<sub>2</sub> layer behaviors more close to monolayers.<sup>[16,17,20]</sup>

First-principle computational approaches based on density functional theory (DFT) were performed to understand the influence of HER reactivity of VS<sub>2</sub> nanosheets induced by the defect and interlayer engineerings. It has been pointed out that the free energy of hydrogen adsorption ( $\Delta G_H$ ) is a good indicator for the activity of the hydrogen-evolving catalysts. Active HER catalysts should have an optimal  $\Delta G_H$  close to zero. Figure 6b shows the calculated free energy diagram for hydrogen adsorption free energy on different VS<sub>2</sub> structures. The insets in Figure 6b and Figure S7 (Supporting Information) show the simulation models for the different VS<sub>2</sub> nanostructures. The defect-rich VS<sub>2</sub> nanosheets with an expanded interlayer spacing of 1.00 nm present the most preferable  $\Delta G_H$  value of -0.044 eV, as compared to those of the defect-rich VS<sub>2</sub> with an interlayer spacing of 0.57 nm ( $\Delta G_H = -0.046$  eV) and the defect-free VS<sub>2</sub> nanosheets with normal interlayer spacing ( $\Delta G_H = 0.366$  eV), as shown from the results in Table S2 (Supporting Information). Therefore, the defect-rich VS<sub>2</sub> (1.00 nm) nanosheets possess optimal catalytic activity. More details of calculation models and parameters can be found in the Supporting Information. In addition, we also calculate the S vacancy

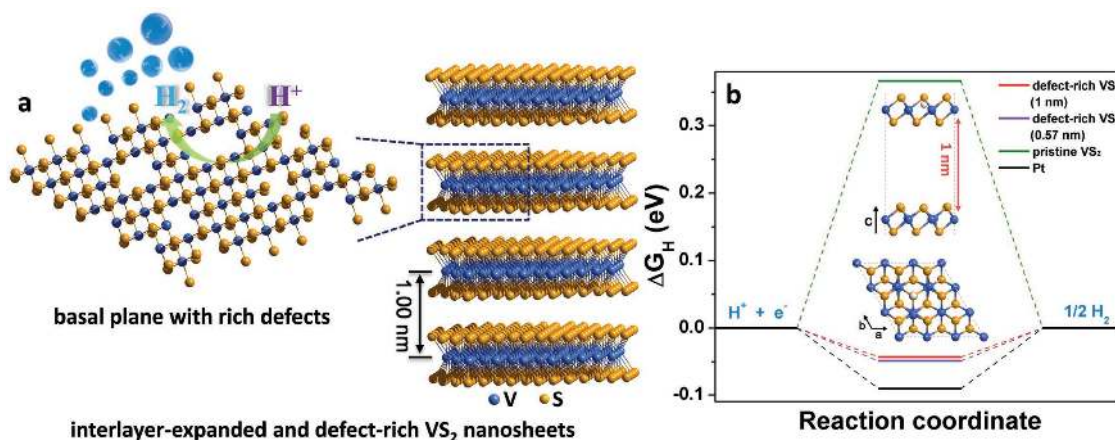


**Figure 6.** a) Schematic illustration of the HER catalytic activity in the freshly prepared solvothermal VS<sub>2</sub> nanosheets with rich defects and expanded interlayer spacing. Blue and yellow balls indicate V and S atoms, respectively. b) Calculated free energy diagram for HER on different VS<sub>2</sub> structures, insets are the VASP models for the defect-rich VS<sub>2</sub> with an expanded interlayer spacing of 1.00 nm. Data of elemental metal Pt ( $\Delta G_{\text{H}} = -0.09$  eV) are taken from the literature report.<sup>[41]</sup> Blue, yellow, and white balls indicate V, S, and H atoms, respectively.

formation energy and find that the energy of defect-rich VS<sub>2</sub> (1.00 nm) is 0.01 eV smaller than that of defect-rich VS<sub>2</sub> (0.57 nm), which suggests that the interlayer-expanded VS<sub>2</sub> is more energetically preferable to form stable vacancy defects during the growth process, further presenting more robust catalytic performance. The calculation results agree well with the above experimental measurements, and the reduced  $\Delta G_{\text{H}}$  of defect-rich VS<sub>2</sub> (1.00 nm) enables a faster HER kinetics, consequently resulting in enhanced HER performance.

### 3. Conclusions

In summary, a facile one-pot solvothermal method is developed to synthesize metallic VS<sub>2</sub> nanosheets with rich defects and expanded (001) interlayer spacing for the first time. The (001) interlayer spacing of the freshly prepared VS<sub>2</sub> nanosheets is as large as 1.00 nm, which shows a 74% expansion. The freshly prepared VS<sub>2</sub> nanosheets exhibit superior HER performance with a low onset overpotential of  $-43$  mV and a small Tafel slope of  $36$  mV dec<sup>-1</sup>, as well as excellent long-term stability, making the interlayer-expanded VS<sub>2</sub> nanosheets a promising low-cost HER electrocatalyst. The improved HER performances of the freshly prepared solvothermal VS<sub>2</sub> nanosheets are attributed to the interlayer expansion and the defect modulation to increase exposed active sites, finally achieving an optimal hydrogen adsorption free energy. Our work opens up a new opportunity to synergistically engineer defects and interlayers of MX<sub>2</sub> nanosheets as efficient HER catalysts.

### 4. Experimental Section

**Synthesis of Defect-Rich and Interlayer-Expanded VS<sub>2</sub> Nanosheets:** A typical procedure for synthesizing VS<sub>2</sub> nanosheets with an expanded interlayer spacing (freshly prepared sample) was performed as follows. Ammonium vanadate (NH<sub>4</sub>VO<sub>3</sub>) (1 mmol) was added to octylamine (20 mL) in a Teflon-lined autoclave (50 mL), and then followed by addition of thioacetamide (CH<sub>3</sub>CSNH<sub>2</sub>) powder (5 mmol). The mixture was magnetically stirred vigorously at room temperature for 60 min.

Afterward, the autoclave was sealed and maintained at 160 °C for 24 h in an oven, and finally cooled down to room temperature. The product was collected by centrifugation and washed with absolute ethanol and distilled water several times, and then vacuum-dried at 60 °C for 12 h.

**Synthesis of the Annealed Solvothermal VS<sub>2</sub> Nanosheets:** The annealed VS<sub>2</sub> nanosheets were prepared by heating the above freshly prepared VS<sub>2</sub> nanosheets at 400 °C for 1 h in a mixed Ar–H<sub>2</sub> (5% H<sub>2</sub>) atmosphere.

**Synthesis of the Hydrothermal VS<sub>2</sub> Nanosheets:** For better comparison and illustration, a sample of defect-rich VS<sub>2</sub> nanosheets with a normal interlayer spacing was also prepared by a hydrothermal synthesis. Typically, Na<sub>3</sub>VO<sub>4</sub>·12H<sub>2</sub>O (3 mmol) and thioacetamide (15 mmol) were dissolved in deionized (DI) water (40 mL). After being magnetically stirring for 1 h, the above solution was transferred into a Teflon-lined stainless steel autoclave (50 mL). The autoclave was sealed and kept at 160 °C for 24 h, and finally cooled down to room temperature. Finally, the product was collected and rinsed with deionized water and absolute ethanol, and then vacuum-dried at 60 °C.

**Characterization:** The crystallographic structures of the various VS<sub>2</sub> samples were characterized by XRD on a Rigaku D/Max-2400 diffractometer with Cu-K $\alpha$  radiation ( $\lambda = 1.54056$  Å) and identified on a Renishaw inVia Raman microscope with an excitation laser beam of 532 nm wavelength. Morphologies, sizes, crystal structures, and compositions were studied with SEM (TESCAN MIRA3), high-resolution TEM (JEOL JEM-2100 at 200 kV), and EDX. XPS was performed in a Thermo ESCALAB 250Xi XPS spectrometer system with a monochromatic Al K $\alpha$  X-ray source (1486.6 eV). TGA and DSC were collected on a Mettler-Toledo TGA DSC 1 Star<sup>e</sup> system under N<sub>2</sub> atmosphere. The surface area was calculated by nitrogen adsorption-desorption isotherms using the BET method on BELSORP-max system (BEL Japan Inc.).

**Electrochemical Measurement:** The electrochemical measurement was carried out in a standard three-electrode configuration on an electrochemical workstation (BioLogic-VMP3), with a saturated calomel electrode as the reference electrode, a Pt foil as the counter electrode, and a glassy-carbon electrode coated with the VS<sub>2</sub> catalysts as the working electrode. Typically, the VS<sub>2</sub> catalyst (5 mg) was added to a mixture of DI water–isopropanol (volume ratio of 3:1) (1000  $\mu$ L) and Nafion solution (5 wt%) (50  $\mu$ L). The mixture was vigorously sonicated for about 30 min to form a homogeneous ink solution. 3  $\mu$ L of the catalyst ink solution (containing 14  $\mu$ g of the catalyst) was then loaded onto a glassy-carbon electrode of 3 mm in diameter with a loading density of about 0.204 mg cm<sup>-2</sup>. The as-prepared catalyst film was dried at room temperature. The electrocatalytic activities of the catalysts were examined by polarization curves using linear sweep voltammetry at a scan rate of 5 mV s<sup>-1</sup> conducted in 0.5 M H<sub>2</sub>SO<sub>4</sub> solution (purged



with N<sub>2</sub> for 30 min). All potentials were carefully calibrated to RHE, and the polarization curves were corrected for iR losses. The EIS spectra were measured with the frequencies from 200 kHz to 0.1 Hz at an overpotential of -55 mV. The chronoamperometry was measured at an overpotential of -55 mV for 60 h (no iR compensation). To estimate the electrochemical active surface areas of the catalysts, cyclic voltammogram curves were tested via measuring C<sub>dl</sub> under a potential window of 0.095–0.345 V at various scan rates (10, 20, 40, 60, 80, 100, 120, 160, and 200 mV s<sup>-1</sup>).

**DFT Calculation:** The first-principle calculations were performed using spin-polarized DFT with the Vienna ab initio simulation package (VASP) code.<sup>[44]</sup> The projector augmented wave potentials were used to describe the core electrons and the generalized gradient approximation of Perdew, Burke, and Ernzerhof was adopted for exchange–correlation functional.<sup>[45,46]</sup> A cut-off energy of 400 eV was used and the tolerance for electron convergence was set as  $1 \times 10^{-5}$  eV while the force tolerance was 0.01 eV Å<sup>-1</sup>. The Brillouin zone sampling was done using a  $12 \times 12 \times 1$  Gamma centered grid for 1T-VS<sub>2</sub> unit cell and a  $4 \times 4 \times 1$  grid for the supercell. A vacuum layer of more than 14 Å was imposed along z direction to prevent interaction between periodic images. And, the DFT-D2 method of Grimme was adopted as approximate vdW correction method.<sup>[47]</sup> Details of the calculation and relevant references are provided in the Supporting Information.

## Supporting Information

Supporting Information is available from the Wiley Online Library or from the author.

## Acknowledgements

This work was financially supported by the National Natural Science Foundation of China (No. 21671096), the Shenzhen Key Laboratory Project (No. ZDSYS201603311013489), the Natural Science Foundation of Shenzhen (Nos. JCYJ20170412153139454, JCYJ20150630145302231, JCYJ20150331101823677), and the Fundamental Research Funds for the Central Universities (No. JZ2016HGTB0725).

## Conflict of Interest

The authors declare no conflict of interest.

## Keywords

hydrogen evolution reaction, interlayer expansion, nanosheets, transition-metal dichalcogenides, VS<sub>2</sub>

Received: September 8, 2017

Revised: November 4, 2017

Published online:

- [1] X. Zou, Y. Zhang, *Chem. Soc. Rev.* **2015**, *44*, 5148.  
 [2] M. Zeng, Y. Li, *J. Mater. Chem. A* **2015**, *3*, 14942.  
 [3] S. Q. Lu, Z. B. Zhuang, *Sci. China Mater.* **2016**, *59*, 217.  
 [4] X. Chia, A. Y. Eng, A. Ambrosi, S. M. Tan, M. Pumera, *Chem. Rev.* **2015**, *115*, 11941.  
 [5] W. Choi, N. Choudhary, G. H. Han, J. Park, D. Akinwande, Y. H. Lee, *Mater. Today* **2017**, *20*, 116.

- [6] S. J. Liu, X. Zhang, J. Zhang, Z. G. Lei, X. Liang, B. H. Chen, *Sci. China Mater.* **2016**, *59*, 1051.  
 [7] D. Voiry, A. Mohite, M. Chhowalla, *Chem. Soc. Rev.* **2015**, *44*, 2702.  
 [8] H. Wang, H. Yuan, S. Sae Hong, Y. Li, Y. Cui, *Chem. Soc. Rev.* **2015**, *44*, 2664.  
 [9] X. Geng, W. Sun, W. Wu, B. Chen, A. Al-Hilo, M. Benamara, H. Zhu, F. Watanabe, J. Cui, T. P. Chen, *Nat. Commun.* **2016**, *7*, 10672.  
 [10] A. Ambrosi, Z. Sofer, M. Pumera, *Chem. Commun.* **2015**, *51*, 8450.  
 [11] G. Ye, Y. Gong, J. Lin, B. Li, Y. He, S. T. Pantelides, W. Zhou, R. Vajtai, P. M. Ajayan, *Nano Lett.* **2016**, *16*, 1097.  
 [12] Z. Lin, B. R. Carvalho, E. Kahn, R. Lv, R. Rao, H. Terrones, M. A. Pimenta, M. Terrones, *2D Mater.* **2016**, *3*, 022002.  
 [13] Y. Yin, Y. Zhang, T. Gao, T. Yao, X. Zhang, J. Han, X. Wang, Z. Zhang, P. Xu, P. Zhang, X. Cao, B. Song, S. Jin, *Adv. Mater.* **2017**, *29*, 1700311.  
 [14] H. Wang, Z. Lu, S. Xu, D. Kong, J. J. Cha, G. Zheng, P. C. Hsu, K. Yan, D. Bradshaw, F. B. Prinz, Y. Cui, *Proc. Natl. Acad. Sci. USA* **2013**, *110*, 19701.  
 [15] D. Kong, H. Wang, J. J. Cha, M. Pasta, K. J. Koski, J. Yao, Y. Cui, *Nano Lett.* **2013**, *13*, 1341.  
 [16] K. D. Rasamani, F. Alimohammadi, Y. Sun, *Mater. Today* **2017**, *20*, 83.  
 [17] Y.-J. Tang, Y. Wang, X.-L. Wang, S.-L. Li, W. Huang, L.-Z. Dong, C.-H. Liu, Y.-F. Li, Y.-Q. Lan, *Adv. Energy Mater.* **2016**, *6*, 1600116.  
 [18] S. Zhang, B. V. R. Chowdari, Z. Wen, J. Jin, J. Yang, *ACS Nano* **2015**, *9*, 12464.  
 [19] J. Xu, J. Zhang, W. Zhang, C.-S. Lee, *Adv. Energy Mater.* **2017**, *7*, 1700571.  
 [20] M. R. Gao, M. K. Chan, Y. Sun, *Nat. Commun.* **2015**, *6*, 7493.  
 [21] M. Jiang, J. Zhang, M. Wu, W. Jian, H. Xue, T.-W. Ng, C.-S. Lee, J. Xu, *J. Mater. Chem. A* **2016**, *4*, 14949.  
 [22] J. Feng, X. Sun, C. Wu, L. Peng, C. Lin, S. Hu, J. Yang, Y. Xie, *J. Am. Chem. Soc.* **2011**, *133*, 17832.  
 [23] J. Feng, L. Peng, C. Wu, X. Sun, S. Hu, C. Lin, J. Dai, J. Yang, Y. Xie, *Adv. Mater.* **2012**, *24*, 1969.  
 [24] X. Fan, S. Wang, Y. An, W. Lau, *J. Phys. Chem. C* **2016**, *120*, 1623.  
 [25] H. Pan, *Sci. Rep.* **2014**, *4*, 5348.  
 [26] Y. Qu, H. Pan, C. T. Kwok, Z. Wang, *Phys. Chem. Chem. Phys.* **2015**, *17*, 24820.  
 [27] H. Liang, H. Shi, D. Zhang, F. Ming, R. Wang, J. Zhuo, Z. Wang, *Chem. Mater.* **2016**, *28*, 5587.  
 [28] J. Yuan, J. Wu, W. J. Hardy, P. Loya, M. Lou, Y. Yang, S. Najmaei, M. Jiang, F. Qin, K. Keyshar, H. Ji, W. Gao, J. Bao, J. Kono, D. Natelson, P. M. Ajayan, J. Lou, *Adv. Mater.* **2015**, *27*, 5605.  
 [29] Y. J. Qu, M. M. Shao, Y. F. Shao, M. Y. Yang, J. C. Xu, C. T. Kwok, X. Q. Shi, Z. G. Lu, H. Pan, *J. Mater. Chem. A* **2017**, *5*, 15080.  
 [30] Z.-T. Shi, W. Kang, J. Xu, Y.-W. Sun, M. Jiang, T.-W. Ng, H.-T. Xue, D. Y. W. Yu, W. Zhang, C.-S. Lee, *Nano Energy* **2016**, *22*, 27.  
 [31] R. Sun, Q. Wei, J. Sheng, C. Shi, Q. An, S. Liu, L. Mai, *Nano Energy* **2017**, *35*, 396.  
 [32] J. Zhang, M. H. Wu, Z. T. Shi, M. Jiang, W. J. Jian, Z. Xiao, J. Li, C. S. Lee, J. Xu, *Small* **2016**, *12*, 4379.  
 [33] X. Chia, A. Ambrosi, P. Lazar, Z. Sofer, M. Pumera, *J. Mater. Chem. A* **2016**, *4*, 14241.  
 [34] N. Alov, D. Kutsko, I. Spirovová, Z. Bastl, *Surf. Sci.* **2006**, *600*, 1628.  
 [35] M. Naguib, J. Halim, J. Lu, K. M. Cook, L. Hultman, Y. Gogotsi, M. W. Barsoum, *J. Am. Chem. Soc.* **2013**, *135*, 15966.  
 [36] Y. Xue, Z. Zuo, Y. Li, H. Liu, Y. Li, *Small* **2017**, *13*, 1700936.  
 [37] A. Anto Jeffery, C. Nethravathi, M. Rajamathi, *J. Phys. Chem. C* **2014**, *118*, 1386.  
 [38] Q. Liu, X. Li, Z. Xiao, Y. Zhou, H. Chen, A. Khalil, T. Xiang, J. Xu, W. Chu, X. Wu, J. Yang, C. Wang, Y. Xiong, C. Jin, P. M. Ajayan, L. Song, *Adv. Mater.* **2015**, *27*, 4837.  
 [39] D. Wang, X. Zhang, S. Bao, Z. Zhang, H. Fei, Z. Wu, *J. Mater. Chem. A* **2017**, *5*, 2681.

- [40] Z. Wu, C. Tang, P. Zhou, Z. Liu, Y. Xu, D. Wang, B. Fang, *J. Mater. Chem. A* **2015**, 3, 13050.
- [41] J. K. Nørskov, T. Bligaard, A. Logadottir, J. R. Kitchin, J. G. Chen, S. Pandalov, U. Stimming, *J. Electrochem. Soc.* **2005**, 152, J23.
- [42] Y. Zhang, X. Chen, Y. Huang, C. Zhang, F. Li, H. Shu, *J. Phys. Chem. C* **2017**, 121, 1530.
- [43] J. Xie, H. Zhang, S. Li, R. Wang, X. Sun, M. Zhou, J. Zhou, X. W. Lou, Y. Xie, *Adv. Mater.* **2013**, 25, 5807.
- [44] G. Kresse, J. Furthmüller, *Phys. Rev. B* **1996**, 54, 11169.
- [45] P. E. Blöchl, *Phys. Rev. B* **1994**, 50, 17953.
- [46] J. P. Perdew, K. Burke, M. Ernzerhof, *Phys. Rev. Lett.* **1996**, 77, 3865.
- [47] S. Grimme, *J. Comput. Chem.* **2006**, 27, 1787.